JOURNAL OF PROPULSION AND POWER
Vol. 26, No. 4, July–August 2010

Heat Flux and Pressure Profiles in an Oxygen/Hydrogen Multielement Rocket Combustor

Mauritz A. deRidder* and William E. Anderson†
Purdue University, West Lafayette, Indiana 47907

DOI: 10.2514/1.48060

Proof of the predictive accuracy of models used in simulation of the high-pressure, high-heat flux environments inside operating rocket combustion chambers is limited by several factors including multiple phases, unsteadiness, high energy release, turbulence, and complex flow geometry. The severe environment also complicates the measurement of temperature, pressure, and chemical composition within the combustor. This paper describes an experiment to collect and analyze benchmark-quality validation data for a multi-element rocket combustor using liquid oxygen and gaseous hydrogen operating at chamber pressures from 300 to 1000 psia at mixture ratios from three to six. For these propellants, the stoichiometric mixture ratio is eight. The combustor was instrumented with 44 coaxial thermocouple pairs to measure axial and circumferential temperature fields and 8 pressure transducers to measure axial pressure profiles. The local heat flux at the inner wall of the combustion chamber computed at each temperature measurement location was found to vary between 4 and 20 Btu/in.^{2}/s. The circumferential variation of heat flux seems to indicate mixing and radial outflow of combustion gases between injector elements, a phenomenon that is not observed in injector configurations with tighter spacing. Further, the axial pressure profiles and head-end temperature measurements suggest the presence of recirculation zones near the injector face.

Nomenclature

a	=	sonic velocity, ft/s
C_d	=	discharge coefficient
c^*	=	characteristic velocity, ft/s
g	=	gravitational acceleration, ft^2/s
k	=	real gas isentropic exponent
L^*	=	chamber characteristic length, in.
P	=	pressure, psia
ρ	=	mass density, lb/ft^3
q	=	heat flux, Btu-in.$^{-2}$-s^{-1}
T	=	temperature, °F
T_w	=	wall temperature, °F
T_b	=	embedded temperature, °F
t	=	time, s
u_α	=	thermal diffusivity uncertainty, ft^2/s
u_q	=	heat flux uncertainty, Btu-in.$^{-2}$-s^{-1}
u_T	=	temperature uncertainty, °F
u_x	=	dimensional uncertainty, in.
Z	=	compressibility factor of hydrogen gas
α	=	thermal diffusivity, ft^2/s

I. Introduction

ROCKET combustion chambers in high-performance liquid propellant engines experience extreme thermal and mechanical loads that increase with increasing chamber pressure and temperature. Unfortunately, these are the primary means of increasing performance in next-generation engine designs. Due in large part to the higher thermal loads on the chamber structure, this performance increase is accompanied by decreased material strength and thus mandates more complex heat management techniques including regenerative cooling, film cooling, injector trimming, and/or injector face biasing. Each of these techniques adds to the complexity of the rocket design and requires much more careful treatment during the design phase. To navigate this shrinking design space and/or produce optimal designs, a comprehensive set of design tools is required. In particular, tools with predictive capability are needed to quickly and accurately select one design over another, reducing the number of expensive and time-consuming hardware tests required.

Although several empirical guidelines exist that are useful in combustor design [1–3], reasonable margins mandate excessive coolant pressure drop, excessive fuel for film cooling, or conservative mechanical design of the chamber wall, all of which degrade the performance of the engine system. More efficient design requires a detailed, high-fidelity understanding of a given engine configuration, which could be accessible from a numerical approach. Computational fluid dynamics (CFD) models have the potential to become an integral part of the engine design process, and their use in the design process is being investigated [4–7].

To be useful, CFD models must be validated against carefully collected experimental datasets. Ideally, these data are obtained using densely instrumented hardware with similar geometry. Such experiments are prohibitively expensive on full-scale engines, so subscale hardware is typically used. Subscale experiments are simpler and safer to operate.

Traditionally, CFD models have been validated using optical techniques such as shadowgraphy, high-speed photography, scattering, absorption, and Raman spectroscopy [8–12]. These techniques are used to ascertain the instantaneous and time-averaged flow properties and/or concentrations of chemical species at a particular location in the chamber. The use of these techniques, however, has some challenging issues for CFD model validation as follows. First, the variables under examination are stochastic in nature and can vary considerably at any point, requiring excessive test and simulation times to build reliable statistics. Second, the test article geometry necessary to accommodate optical access tends to be nonrepresentative of actual combustors due to window mounting and cooling requirements. Third, at very high pressures optical signals can be severely degraded due to nonuniformities in the refractive index resulting from partial combustion, multiphase flow, and trans and/or supercritical environments. Despite these shortcomings, several techniques have been successfully used for the validation of CFD models, and these site-specific data can be valuable. Planar laser-induced fluorescence imaging of OH radicals and Raman scattering, for example, have been employed with great reliability as a flame marker and temperature probe. These techniques enable

Received 9 November 2009; revision received 25 April 2010; accepted for publication 25 April 2010.

*Postdoctoral Researcher, Aeronautical and Astronautical Engineering. Member AIAA.

†Associate Professor, Aeronautical and Astronautical Engineering. Member AIAA.

optical examination of flows with low particulate content and low luminosity that are otherwise problematic.

The alternative to optical or other point-measurement techniques is to measure a time-integrated quantity such as the heat flux. Recent progress in CFD model development [5,6,13–15], validation efforts [7,16,17], and subscale experiments [18–24] all suggest that a combination of surface and integral quantities can serve as a very promising method of CFD validation and that significant confidence is gained in the validation effort with varied operating conditions. It has been noted [25] that the heat flux may provide a more appropriate validation parameter for CFD models than species concentration or local temperature alone. This is due to the following reasons. First, the use of an integrated quantity includes information about the history of the experiment. In this case, the time history of the heat flux is a measure of the time history of the wall temperature. Second, the inclusion of a field variable such as the temperature and its derivative in a conjugate CFD model enhances the confidence that the gradients away from the boundary are correctly modeled. The disadvantage of this technique is that high-frequency components of the heat flux are suppressed by the time required for thermal energy to diffuse through the chamber wall.

The most relevant single-element experiments measuring heat flux conducted to date are those directly involved with the multiscale validation effort conducted by Jones et al. [22,26]. These tests collected benchmark-quality heat flux data from a combustion chamber with a recessed shear-coaxial injector element using liquid oxygen and gaseous hydrogen propellants. Marshall et al. also conducted analogous experiments using a gas–gas combustor [24].

A review of the data collected by Marshall et al. [24] and Jones et al. [22,26] leads to several conclusions. First, the heat fluxes peak in the upstream portion of the chamber followed by a gradual decrease toward the convergent section. This suggests that rapid mixing and most of the combustion takes place in the forward end of the thrust chamber [27]. Thus, Jones et al. recommended that future experiments should cluster instrumentation more closely near the injector face. Second, Marshall et al. report that scaling the wall heat flux by chamber pressure raised to the power 0.8 results in collapse of the axial heat flux profiles to a single group. The data collected by Jones et al. contradict this; their reported wall heat flux profiles collapsed to two groups.

Several previous studies on multi-element hardware have been performed but do not report results for circumferential variation of heat transfer through the combustor walls. Schacht et al. conducted a series of tests on a 234-element LOX/GH_2 combustor with five thermocouple locations axially from the head end of the chamber to the nozzle exit [28]. Their heat flux derivations, however, were obtained by integrating the analytic solution for a constant heat flux. The application of constant heat flux approximations to a transient problem in this way has since been shown to be inaccurate [29]. Additionally, they collected an insufficient amount of data to validate CFD models at multiple locations within the chamber. Quentmeyer et al. studied a similar combustor, with 270 shear coaxial LOX/gH_2 elements and 21 copper rod calorimeters [30]. This combustor employed film cooling to prolong test duration, which complicated the heat transfer analysis at the chamber wall. These experiments were run at conditions that closely approximated the actual operating conditions of their target engine; off-nominal conditions were not investigated. The accuracy of CFD model validation, however, increases with increasing range of operating conditions [31]. Additionally, Arnold et al. reported the geometric distribution of heat flux in multi-element combustors modeled after the Vulcain-2 to determine the effectiveness of film cooling and determine the low-cycle fatigue characteristics of rocket chambers [32].

The use of time-integrated quantities such as heat flux with surface point measurements provides sufficiently detailed boundary conditions for CFD model validation [16,31,33,34]. To that end, the present experiment aims to collect temperature data at both the inner surface and embedded within the combustion chamber wall suitable for heat flux determination. The thermocouples are placed most densely in regions of the chamber where the highest gradients are expected: near the injector face and inline with the injector elements. Forty-four pairs of coaxial thermocouples and eight high-accuracy pressure transducers were installed into a rocket combustion chamber with seven LOX-centered shear-coaxial injector elements. A detailed description of the experimental setup is provided in the next section.

The determination of heat flux from discrete temperature measurements is discussed, including an overview of the method used. The heat flux profiles derived from the temperature measurements are presented in abridged form, as are selected data from thermocouples installed in the injector face. From these data several qualitative insights into flow within the chamber are evident, such as impingement locations of injector plumes, recirculation zones, and regions of strongly three-dimensional flow. Further, the quality of CFD validation can be determined using uncertainties in both the experimental data and CFD model [17,35]. This requires a detailed uncertainty analysis of the experimental data.

II. Experimental Setup

A. Chamber Design

A cutaway view of the chamber is shown in Fig. 1. The overall length is 12 in with an inner diameter of 2.68 in. The wall thickness is 1.66 in. With the nozzle attached, the combustion chamber's total length is 13.5 in and has a characteristic length L^* of 67.6 in. This value was chosen to correspond with previous single-element experiments [19,20].

The coaxial thermocouples used in this experiment are manufactured by Medtherm, Inc. of Hunstville Alabama (Product No. TCS-099-TT-0.250-0-6-11424). Consisting of a pair of type T thermocouples mounted 0.250 in apart, this thermocouple plug design and ones very similar have been used in previous experiments [26]. The core of the thermocouple assembly is a copper cylinder with a constantan wire threaded through the center. A junction is created at the end of the cylinder by abrading the surface gently with emery paper. The second junction is created at the other end of the copper cylinder. This thermocouple assembly is press-fit into an oxygen-free high-conductivity (OFHC) copper plug, the end of which is machined to match the inner diameter of the chamber as shown in Fig. 2.

In addition to temperature profiles, an axial static pressure profile and two high-frequency pressure measurements at the injector face are also included in the combustion chamber instrumentation. To capture the axial pressure profile, a series of eight high-accuracy pressure transducers (Druck PMP 4060, 3000 psia, 0.4% full-scale

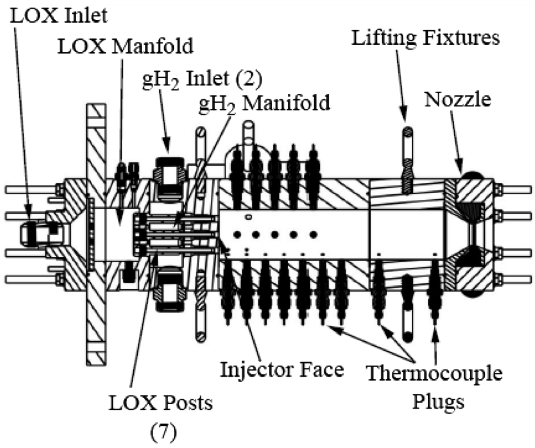

Fig. 1 Cutaway view of the combustion chamber and seven-element injector. The chamber length and diameter are 12 and 2.66 in., respectively. Forty-one pairs of coaxial thermocouples were installed in plugs in the chamber wall upstream of the convergent section. Three thermocouple pairs were press-fit into the injector face. P_c was varied from 300 to 1000 psia and mixture ratio varied from 3 to 6. The chamber, injector, and nozzle were fabricated from OFHC copper. The LOX posts and mounting hardware were fabricated from type 304 stainless steel.

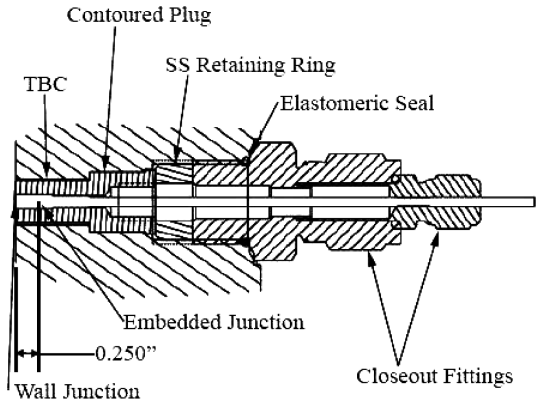

Fig. 2 Thermocouple plugs were designed to closely approximate an insulated cylinder heated at one end. Thermal insulation was provided by a flame-sprayed zirconium oxide layer around the circumference of the plug before installation into the chamber. The end of each plug was contoured to match the inner chamber surface.

error) were installed in the chamber. As with the thermocouples, they were clustered more densely near the injector face. Additionally, a pair of Kulite WCT-312 high-frequency pressure transducers were installed near the injector face. These transducers were mounted in recessed regions designed with their acoustic resonances far from the L1 and L2 modes of the chamber. The transducers were water-cooled throughout the tests and sampled at 200 kHz. The layout of instrumentation in the chamber is shown in Fig. 3.

The nozzle is fabricated from copper and is water-cooled at a pressure of 800 bar with 28 lb/s of water. At the highest heat flux case, the maximum water temperature rise through the nozzle over the entire test was 5°F.

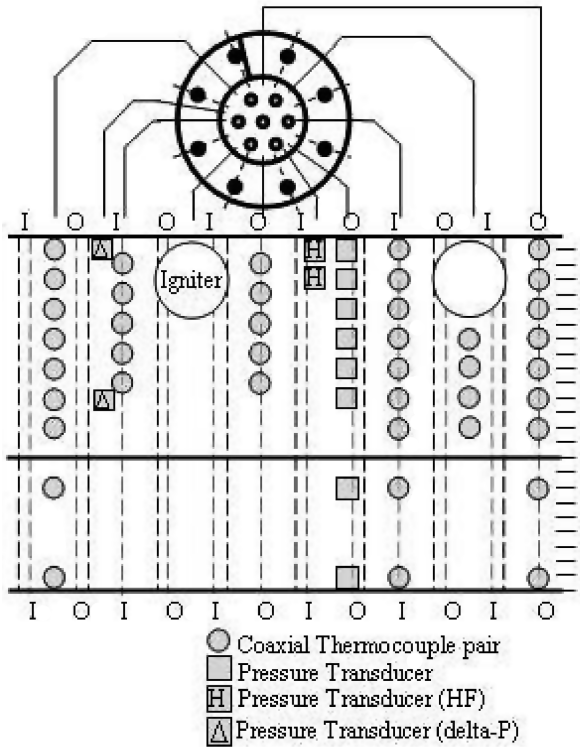

Fig. 3 Instrumentation layout. Axial rows of thermocouples are places inline with injector elements, offline (equidistant from two injector elements) and between the inline and offline positions. In addition, a row of high-accuracy pressure transducers and two high-frequency pressure transducers were installed. A differential pressure transducer installed across the chamber failed on the first test, and was not replaced.

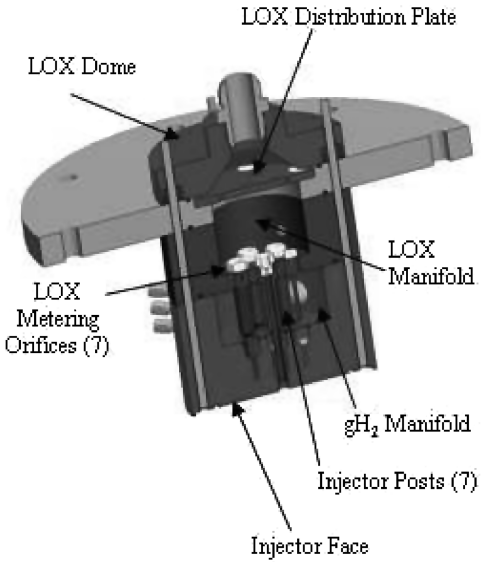

Fig. 4 Injector overview. LOX flows from the inlet at the top of the figure through the distribution plate into the manifold. The distribution plate contains 114 holes spaced to evenly distribute fluid flow over all seven elements and break up direct impingement of fluid jets on the LOX metering orifices in the manifold. The metering orifices provide the same flow rate of LOX to each injector post.

B. Injector Design

The injector, shown in Fig. 4, consists of seven liquid oxygen (LOX)-centered, recessed shear-coaxial posts fabricated from type 304 stainless steel. The fuel ports are on the side of the manifold, and hydrogen enters the combustion chamber through concentric annuli around the LOX posts. The design of the posts and hydrogen annuli was targeted to provide uniform, one-dimensional flow of both propellants to the chamber to simplify the boundary conditions for CFD model validation. The posts were elongated and the hydrogen flowpath stepped down from a larger diameter to smaller in a series of ramps to cancel out any tangential or radial velocity components. Before assembly, the injector's flow characteristics and pressure drops were determined using water and nitrogen gas as propellant simulants.

C. Injector Design

A total of 19 tests were conducted, of which 12 tests were unique and seven tests were repeats. The complete test matrix is shown in

Table 1 Test matrix

Test	Target		Actual				Repeat
	P_c, psia	O/F	P_c, psia	O/F	O_2, lbm/s	H_2, lbm/s	
24	800	3	823.4	2.86	2.49	0.866	24,25,59
25	800	3	823.1	3.03	2.50	0.843	24,25,59
26	600	4.5	630.5	4.11	2.08	0.507	26,56,57,58
41	300	6	333.2	4.77	1.13	0.234	41,53
42	300	4.5	332.6	3.92	1.08	0.274	——
43	300	3	313.5	2.52	0.91	0.361	——
46	1000	4.5	982.2	4.46	3.37	0.758	——
47	1000	6	967.1	6.46	3.71	0.574	——
48	1000	3	1011.7	2.94	3.04	1.034	——
49	800	6	819.6	5.75	3.02	0.526	——
50	800	4.5	811.8	4.30	2.70	0.625	——
52	600	3	640.7	2.79	1.83	0.655	——
53	300	6	329.8	4.80	1.14	0.231	41,53
54	600	6	633.6	5.66	2.28	0.402	——
55	600	6	629.3	5.99	2.30	0.385	——
56	600	4.5	609.4	5.03	2.08	0.419	26,56,57,58
57	600	4.5	597.0	5.07	2.06	0.406	26,56,57,58
58	600	4.5	646.3	3.59	2.00	0.570	26,56,57,58
59	800	3	808.7	3.04	2.40	0.795	24,25,59

Table 1, which contains the target and actual test conditions. Several tests were repeated in an attempt to better match the target conditions, and others were performed to monitor hardware degradation. There are three such hardware repeatability pairs: 1) test 59 is a repeat of test 25, 2) test 58 is a repeat of test 26, and 3) test 53 is a repeat of test 41. These were spaced such that one of the first three tests was repeated at the beginning, middle, and end of the test campaign. All the tests in this campaign were run below the stoichiometric mixture ratio of eight. The liquid oxygen propellant system has a liquid nitrogen heat exchanger just upstream of the run tank, which ensures the availability of subcooled LOX over the entire experiment.

The mass flow rates reported were determined from pressure measurements upstream of the cavitating and critical flow venturis used to meter the LOX and gH_2 propellants. A calibration effort was undertaken to measure the uncertainty in C_d value for each venturi. Results suggest that the maximum uncertainty in the venturis used in the current experiment was $\pm 2.5\%$. The compressibility factor Z is a thermodynamic property to account for the real gas behavior of hydrogen, and is modeled in SI units to an accuracy of 0.04% by Lemmon et al. [36].

The isentropic exponent k is poorly approximated by the ratio of specific heats at elevated pressures, and is better modeled by the relation in Eq. (1) [37] where a and ρ are the sonic velocity and density, respectively, and are determined from National Institute of Science and Technology (NIST) lookup tables. As usual, g is the gravitational constant

$$k = \frac{1}{144}\frac{\rho a^2}{Pg} \tag{1}$$

III. Heat Flux Determination

The heat flux probes used in this study are similar to those used on previous investigations [38], and consist of a pair of coaxial thermocouples embedded within a cylindrical copper plug; their design is discussed further in a previous section. All the heat flux data presented were reduced using a one-dimensional forward conduction model in which the boundary and initial conditions are known and the heat flux determined by differentiation of the field variable. The spatial and temporal discretization of the differential equation was performed using the numerical differentiation formulas and Runge–Kutta methods to produce estimates of the solution at successive times [39,40]. Briefly, this is a second-order-accurate piecewise nonlinear Galerkin/Petrov–Galerkin method. It is applicable for any differential equation that can be cast into the form of Eq. (2) with boundary conditions of the form in Eq. (3) at boundaries a, b

$$D(x,t,u,u_x) = x^{-m}(x^m g(x,t,u,u_x))_x + f(x,t,u,u_x) \tag{2}$$

$$p^i(x,t,u) + q^i(x,t)g^i(x,t,u,u_x) = 0 \tag{3}$$

With the governing differential equation cast into this form, it is possible to integrate by parts and obtain the integral equation in Eq. (4), which can be readily solved using numerical quadrature [40]

$$-\int_a^b x^m g \psi_{ax}\,\mathrm{d}x = a^m v(a) + \int_a^b Q x^m \psi_a\,\mathrm{d}x \tag{4}$$

This formulation requires that one thermocouple be at the heated surface and that both thermocouples be functioning throughout the entire test. Either Neumann or Dirichlet boundary conditions can be used to compute the temperature distribution. The temperature histories of the thermocouples or the wall heat flux at the inner surface can be imposed as boundary conditions. In both cases the (uniform) initial temperature of the wall is used as an initial condition. To mitigate the effects of noise on the heat flux estimate, the raw temperature data was filtered. For all tests a 21-point, fourth-order Savitsky–Golay filter was applied to both the wall and embedded thermocouple data before the data were fed into the data reduction code.

To verify the accuracy of the forward model both sample data and a subset of experimental data were reduced using an inverse technique, zeroth-order Tikhonov regularization [29,41–43]. The data reduction code produced sufficiently accurate estimates of heat fluxes for the sample data cases, including the step and triangle heat flux inputs which are generally regarded as the most stringent [29].

IV. Experimental Results

A. Chamber Thermocouple Data

A set of typical temperature traces from functioning thermocouples is shown in Fig. 5. There are several features directly observable in the plot. Initially, the chamber has been cooled by a liquid oxygen prechill, so some wall thermocouples report low temperatures in the chamber. Second, there is a small spike in a few wall temperature traces before main chamber ignition. This is caused by the presence of combustion products from the igniter passing through the chamber. The main chamber ignition event is signaled by a rapid rise in wall temperature. Because the chamber is heat-sink cooled, the wall temperature does not reach steady-state conditions. Typically, test times were limited by the recommended thermocouple limit of 1000°F. The shutdown event is heralded by a sharp point and rapid falloff of the wall temperatures, followed by a slow decay back to the ambient temperature. Temperature traces of all the wall thermocouples for test 49 are shown as dotted lines on Fig. 5. The spread of the wall temperatures is due to varying position within the chamber. The data from the embedded thermocouples are omitted from the figure for clarity. They are similar to the wall data but respond more slowly and with smaller magnitude due to the thermal mass of the inner portion of the chamber wall. The solid line is the Bartz estimate of wall temperature assuming transient conduction through an infinite wall. The estimate overpredicts wall temperatures near the nozzle and underpredicts temperature near the head-end of the combustor.

B. Face Thermocouple Data

The three coaxial thermocouples installed in the injector face successfully recorded data for all tests with the exception of test 25. Their position relative to each other and the injector elements is shown schematically in Fig. 6. The temperature and heat flux results from all three thermocouple pairs for test 59 are shown in Figs. 7 and 8, respectively.

Thermocouple 3 is closest to the inner chamber wall and is directly opposite the igniter. The impingement of igniter exhaust on the opposite side of the chamber can be clearly seen in the temperature and heat flux traces of Figs. 7 and 8. The peak temperature during igniter operation was highest for thermocouple 3 and lowest for thermocouple 1. This trend was reversed for main chamber

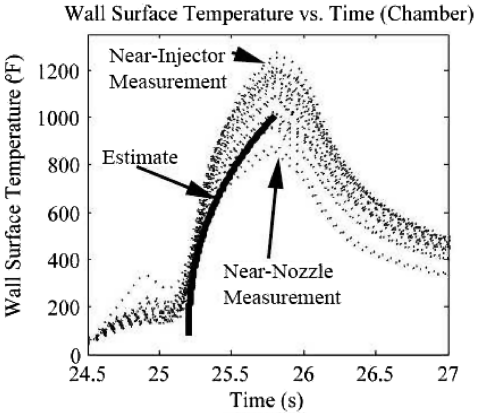

Fig. 5 Wall temperature data for test 49; $P_c = 967$ psia, O/F = 6.46. The wide range of maximum temperatures is due to the geometric variation of thermocouple placement: those nearest the injectors experienced much higher temperatures than those farthest from the injector face. Included is the Bartz estimate of chamber wall temperature at these conditions.

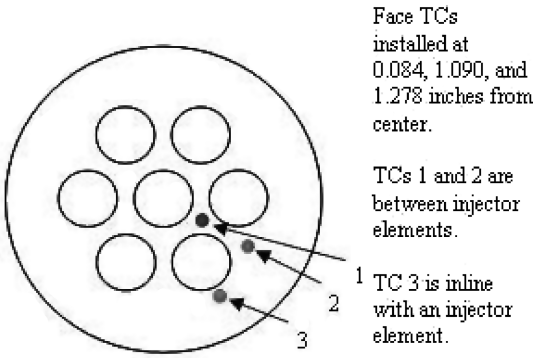

Fig. 6 Injector face thermocouple (TC) layout, viewed from nozzle. The three coaxial thermocouples are press-fit into the injector face from the interior of the hydrogen manifold at the locations shown. The igniter is mounted on the top left of the image, and impinges very near the position of TC 3.

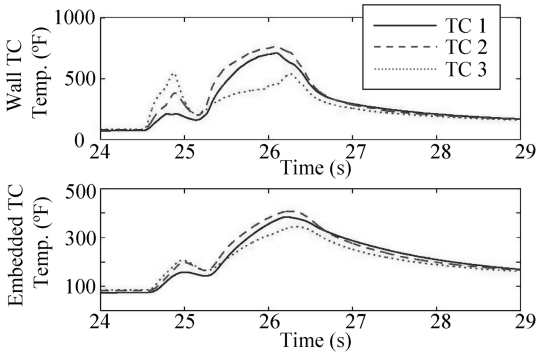

Fig. 7 Injector face temperature data for test 59; $P_c = 808.70$, $O/F = 3.09$. The upper plot shows wall temperature traces for the three thermocouples. The lower plot shows the embedded temperature measurements. Visible in both plots is the peak before 25 s due to igniter combustion, followed by main chamber ignition. The igniter was mounted directly opposite from TC 3. Consequently, this location shows the highest temperatures during igniter operation.

operation. The thermocouples nearest the center of the injector face experienced higher heat loads than the thermocouple near the wall. This suggests the presence of a recirculation zone between the outer row of elements and the combustor wall.

Inspection of the heat fluxes yields the same conclusions as the temperature data. The thermocouple closest to the wall experienced higher heat fluxes during igniter operation due to its proximity to the igniter impingement. During main chamber operation, this thermocouple experienced lower heat flux loads. For these test

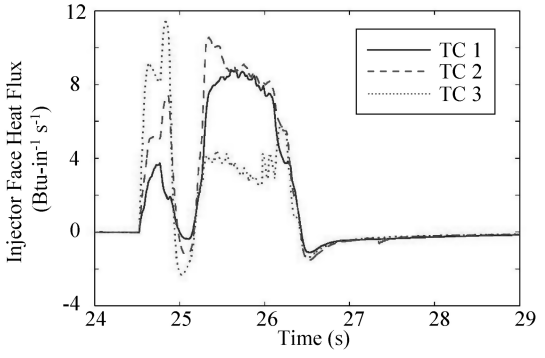

Fig. 8 Injector face heat flux for test 59; $P_c = 808.70$, $O/F = 3.09$. As with the temperatures shown in Fig. 7, the near-wall TC shows the highest flux during igniter operation due to igniter combustion product impingement. During main chamber operation this location was considerably cooler, possibly due to the presence of a recirculation zone between the injector element and the wall.

conditions, Bartz' approximations produce an estimate of wall heat flux of between 10.2 and 10.9 Btu/in.^{2}/s. This estimate is close to the actual values observed at thermocouple locations 1 and 2, suggesting that Bartz' equation is appropriate for use at interior locations of the injector face, but not near its edges or other locations where complex recirculating flow may be present.

C. High-Accuracy Pressure Measurements

Because of the structure of the data acquisition apparatus in the current work, the main chamber pressure transducer and the high-accuracy chamber pressure transducers were recorded on separate data systems. The main pressure transducer was used to initiate aborts, if necessary, and for real-time monitoring of the test. High-frequency measurements using eight high-accuracy transducers were recorded and stored for later analysis. A typical set of axial profiles of pressure at early and late inspection times is shown in Fig. 9. The early time corresponds to the maximum heat flux experienced in the chamber. The late time was just before shutdown and represents close to a steady-state condition. Each pressure data point shown is averaged over a 150 ms window. The farthest downstream transducer, at 11.5 in., displayed a nonlinear calibration and was removed from the dataset.

The uncertainty in these pressure measurements is either 0.04% of their full-scale range or the uncertainty due to differences in the pretest and posttest calibration, whichever was larger. As shown in Fig. 9, for all the transducers except those at 3.5 and 4.5 in., the uncertainty was 2 psi. For the remaining two, the uncertainties are 3 and 4 psia. Inspection of the pressure data prevents conclusive observations as most of the variation in the axial pressure profiles is within this uncertainty. With this restriction, however, some things can still be seen. There is a steep pressure rise near the head-end of the chamber. This is in the same region in which the highest chamber temperatures and heat fluxes were recorded, which is consistent with rapid heat release near the injector face. Toward the nozzle, the combined effects of heat loss to the walls and acceleration of the flow keep the chamber pressure within the uncertainty of the measurements. Additionally, as the chamber wall temperature climbs toward the end of the test, the pressure profile is increasingly dominated by the acceleration effect. This is demonstrated by the decreased pressure profile at the late time point.

The chamber and propellant manifolds were instrumented with Kulite high-frequency pressure transducers for several tests. These instruments were included to address stability concerns and to aid in mitigating any instability observed. The high-frequency oscillation amplitudes were less than 5% of the mean chamber pressure for all tests that were instrumented with the high-frequency system.

D. Spatial Variation of Heat Flux

The heat fluxes reported in this and the following sections were reduced from the temperature data and fitted with a smoothing spline using a weighted penalty method. Axial profiles of heat flux for high, medium, and low heat flux cases are shown in Fig. 10. As expected, heat flux increases dramatically with increasing chamber pressure in

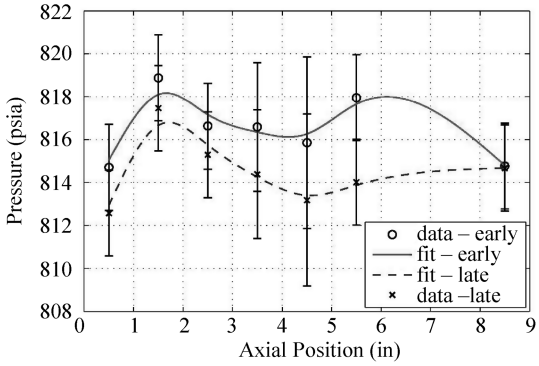

Fig. 9 High-accuracy pressure data for test 25; $P_c = 823.11$, $O/F = 3.03$.

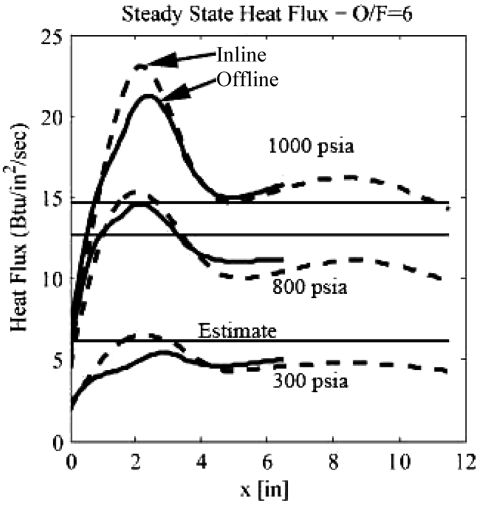

Fig. 10 Heat flux profiles for several cases. Horizontal lines are Bartz estimates of heat flux computed using frozen gas composition. The point at $x = 0$ refers to measurement on injector face. Solid lines are heat flux profiles at circumferential locations equidistant from two injector elements (offline position), dashed lines are heat flux profiles at locations directly inline with injector elements (inline position).

accordance with expectations from Bartz' estimate. Further, locations inline with the injector elements experienced the highest heat flux while those furthest from the injector elements experienced the least. Many of the profiles in the dataset exhibit a similar form to those in Fig. 10. The flux is a maximum 1–2 in. downstream from the injector face and falls off slowly toward the nozzle. Generally, the maximum heat flux occurs farther upstream for locations near the injectors (inline position) than elsewhere in the chamber.

Similar plots for four test conditions are shown in Fig. 11. From the plots, it seems that the recirculation zone extends between one and 3 in. downstream from the injector face. From the offline heat flux profile, possible combustion gas impingement appears to occur further downstream. This may indicate mixing of the injector streams and the radial flow outward of combustion products. This strongly suggests three-dimensionality of the flowfield, and implies that CFD models intending to capture accurately the behavior of multi-element chambers must account for such flow.

These data contain several interesting features. First, the location of maximum heat flux is within the first 2 in. downstream of the injector face. This is much shorter than the distance observed in heat-effect marks on the inner surfaces of other combustors [29] and in the single-element data. This may be due to several factors including more rapid mixing due to three-dimensionality of the flowfield or interaction between injector flows. In the current work, the spacing from the outer row of elements to the chamber wall is larger than in a conventional combustor, largely to facilitate comparisons with the single-element chamber. This spacing may contribute to the formation of a recirculation zone within the chamber. Further evidence of this can be found in the surface temperature measurements at the 0.5 in. location inline with the injector and the nearest injector face measurement. Both are significantly cooler than the surrounding thermocouples. This may indicate that entrained hydrogen gas is providing local cooling to the walls at the head-end of the chamber. Second, the dual-peak nature of the heat flux, one inline and one offline at a separate location, is unique. This behavior has not been previously documented through direct measurement. It suggests that the plumes from adjacent injectors are mixing and their combined plume has a significant radial component.

V. Uncertainty Analysis

All propellant flows were metered using critical flow and cavitating venturis. A comprehensive uncertainty analysis was performed for the facility, which included an analysis of these venturis. The component uncertainties of discharge coefficient C_d and area A were measured and a combined uncertainty in their product was computed using a conventional catch-and-weigh technique. The results indicated that the maximum combined uncertainty was approximately 5%. The density ρ and vapor pressure P_v are determined from a lookup table of NIST-tabulated data. The propagation of uncertainty for the table lookup procedure was performed per standard practice. The lookup temperature and pressure uncertainties are given by the manufacturers of the sensors (e.g. 5 psi for the Sensotec TJE pressure transducers and 4°F for the thermocouples). The uncertainty in the underlying data is provided by NIST[‡]. For all the tests in this series, the mass flow rate uncertainty was less than 5%.

As described above, the heat flux is computed by solving the heat diffusion equation using the numerical differentiation formulas; no closed-form solution exists for the unknown heat flux. For this reason, traditional error propagation is impossible. However, once the field variable $T(x, t)$ is known, the heat flux $q(t)$ is determined by simple differentiation and can be written as

$$q(t) = \alpha \frac{\partial T(0,t)}{\partial x} = \alpha \frac{T_2 - T_1}{x_2 - x_1} \tag{5}$$

The quantities T_i and x_i are the nodal temperatures and locations, respectively. Propagating the relative uncertainty u_q/q results in an estimate of the heat flux uncertainty, which is given as

$$\frac{u_q}{q} = \sqrt{u_a^2 + \frac{T_w^2 u_{Tw}^2}{(T_w - T_b)^2} + \frac{T_b^2 u_{Tb}^2}{(T_w - T_b)^2} + \frac{x_2^2 u_x^2}{(x_2 - x_1)^2} + \frac{x_1^2 u_x^2}{(x_2 - x_1)^2}} \tag{6}$$

The quantities u_{Tw} and u_{Tb} are the uncertainties in the wall and embedded temperatures, respectively. Equation (6) shows that the uncertainty in heat flux is a strong inverse function of the temperature difference between the thermocouples. As this quantity approaches zero, the uncertainty in heat flux grows without bound. However, the heat flux itself also becomes extremely low when the temperature difference approaches zero. This low heat flux value is not in the scope of the current work. The heat flux is of most interest during main chamber combustion, in which case the wall thermocouple will be heated much more strongly than the embedded thermocouple, so the difference in their temperatures should be relatively large. The only exception to this expectation is during thermal soakback. During this time, the inner surface of the combustor is no longer heated and is cooled by the purge gases flowing through the chamber. This effectively reverses the direction of heat flow in the chamber wall, which results in a condition where the embedded thermocouple is warmer than the wall thermocouple.

The heat flux uncertainty is also a function of the uncertainty in the thermal expansion coefficient of the wall material u_α. The wall property value used in the current work was obtained from the work of Esposito and Zabora [44] on thrust chamber life prediction, but the uncertainty in these values was not addressed in the work. To estimate the material property uncertainties, it is useful to consult White and Minges [45] survey of a wide range of properties, including the thermal expansion coefficient, heat capacity, and thermal conductivity of OFHC copper reported in the literature. They found large variations in material properties among different studies. These discrepancies have yet to be explained, but seem to be dependent on the particular copper specimen used. These variations must be taken into account for the current multi-element experiment because the combustion chamber and the thermocouple plugs were not fabricated from the same piece of copper stock. More important, the copper plugs themselves were not machined from the same piece of stock; at least two different specimens were used and no material fabrication records were kept. This implies that there may be

[‡]Data available online at http://webbook.nist.gov [retrieved 21 February 2009].

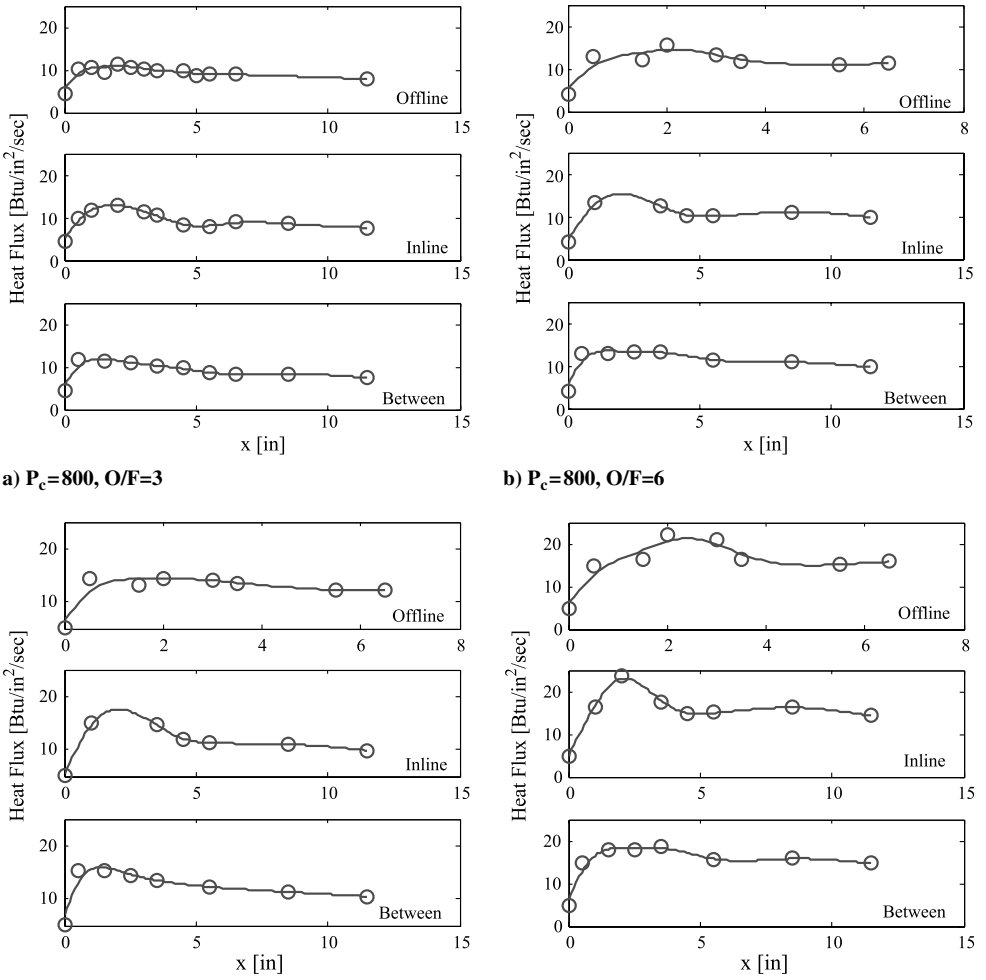

Fig. 11 Heat flux profiles for varying test conditions.

variations in material properties of the thermocouple plugs similar to that observed by White and Minges (e.g., 5% in thermal conductivity, and 2.5% each in heat capacity and density). Overall, the material property uncertainties result in a relative uncertainty in computed heat flux of 5.9%. For example, test 25 yielded an absolute uncertainty of 0.8260 Btu/in.^{2}/s on a 14 Btu/in.^{2}/s heat flux as shown in Fig. 12.

Second, the design of the embedded thermocouple prevents absolute assurance of uniformity across sensors. The wall thermocouple junction is fabricated by slivering the constantan wire to a copper sheath, while the embedded thermocouple junction is welded. This weld is performed perpendicular to the thermocouple axis, so the constantan wire must be bent and wrapped around the copper core before welding. These processes are performed by hand, and increase the uncertainty of the location of the embedded junction.

Finally, the installation of the thermocouples within the plug and the plug assembly in the chamber may result in slight variations in chamber surface condition. Those thermocouples that are slightly recessed may experience different heat fluxes compared with those that are flush or that protrude slightly.

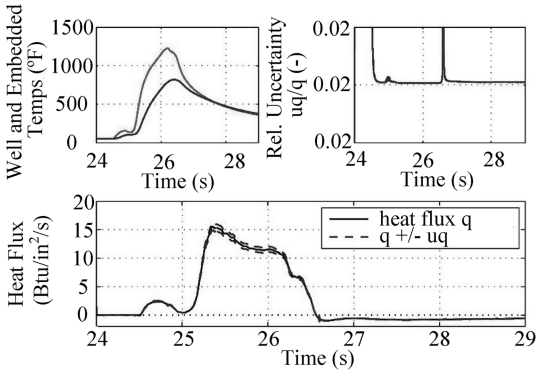

Fig. 12 Temperature, uncertainty in heat flux, and heat flux for test 25.

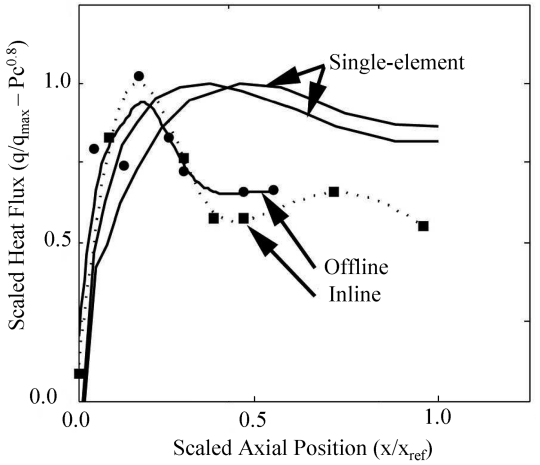

Fig. 13 Scaled heat flux profiles: P_c = 800 psia. Normalized inline and offline measurements are shown, as well as normalized single-element data from Jones et. al. [22,26] at similar test conditions.

VI. Comparison with Other Studies

The heat flux profiles observed in this experiment are slightly different than those from the single-element cases. As shown in Fig. 13, the normalized single-element heat flux profiles rise gradually with distance from the injector. They do not exhibit the sharp peak in heat release observed in the multi-element cases. This difference may be due to enhanced mixing through injector-injector interaction and/or the presence of recirculation zones near the injector face in the multi-element cases. Additionally, multi-element data from a subscale combustion chamber studied by Arnold et al. [32] are plotted in Fig. 14. These data show that the heat flux rises continually to the convergent section of the nozzle. Several features of this chamber are worth noting. First, Arnold's chamber is water cooled, whereas the chamber used in the present study is heat-sink cooled. Water-cooled hardware can reject significantly more heat, which enables true steady-state conditions. This difference has a significant effect on both the flowfield near the injector face and the wall temperature. Second, the injector head in Arnold's chamber is modeled after a realistic engine injector and has a greater number of elements that are spaced close together. The injector element spacing in the present study was patterned after the single-element tests of Jones et al. [22,26] and Marshall et al. [24], and has only seven widely spaced elements. Together, these result in a more even lateral propellant distribution in Arnold's chamber. As a result, these two chambers have different mixing characteristics and dramatically different heat flux behaviors.

The discrepancy between the multi-element tests and their single-element analogs is largely attributable to enhanced three-dimensional mixing of the propellants. This mixing is promoted by injector–injector interactions that are not present in the smaller chamber. Additionally, the single-element heat flux profile were computed assuming that the injector face heat flux is zero.

The multi-element data from the chamber investigated by Arnold et al. [32] are markedly different from the multi-element chamber used in the current work. The monotonic rise in heat flux toward the nozzle was not seen in this experiment. Care must be taken with this comparison, however, as the subscale combustion chamber model E BKE chamber is water cooled and has a characteristic length of approximately 8 in., which implies that the combustion efficiency, and the underlying combustion flowfield, may be quite different. This difference is encouraging from the standpoint of CFD model validation, however, as a model that can capture both behaviors with only geometric changes gains a significant boost in confidence.

The heat flux trends in the chamber vary most notably with the chamber thermal condition, which varies throughout the test. Early in the test, the bulk of the chamber wall is still cool, so thermal gradients are largest. This is the time when the largest heat fluxes are observed. Later in the test, as the wall temperature rise slows and the bulk of the wall material warms up, the heat flux also lessens. Normalization of axial heat flux profiles at these two times reveals two distinct behaviors. Early in the experiment, near their maximum values, the axial heat flux profiles collapse to two distinct groups when scaled by $P_c^{0.8}$. Late in the test, the scaled axial profiles collapse to a single group with a larger range. Thus, it is crucial for experimentalists to define precisely the portion of experimental data used when reporting heat flux values.

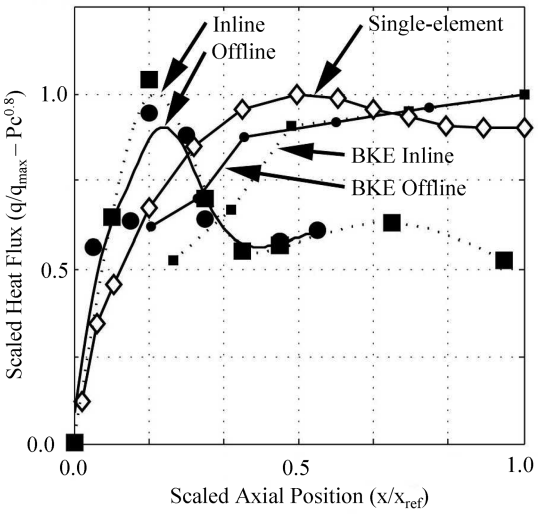

Fig. 14 Scaled heat flux profiles: $P_c = 1000$ psia. Normalized inline and offline measurements are shown with normalized multi-element data from Arnold et al.'s chamber [32], as well as normalized single-element data from Jones et. al. [22,26] at similar test conditions.

Table 2 Fit coefficients

A	0.085
B	0.811
C	−1.182
D	2E − 7
E	−0.828

The maximum heat flux in the chamber occurred between 2 and 5 in. downstream of the injector face for all tests, regardless of circumferential position or sampling time. This maximum was highest at circumferential positions inline with injector elements, and lowest between elements. These differences in heat flux profiles suggest several physical phenomena that may be at work. First, the presence of recirculation zones in the injector element planes is suggested the sharp rise in heat flux in the first 1–2 in. downstream of the injector face at the inline position. This rise is not present in the offline or between heat flux profiles, suggesting that the recirculation zones may be circumferentially separated. Second, the peak in heat flux in the offline heat flux profiles from 2 to 4 in. downstream is without an analog at the inline position. Because there are no propellant sources in this location the presence of radial flow outward, possibly generated by the merging of injector plumes, is suggested.

The maximum heat flux in the chamber was nearly independent of mixture ratio, and varies with chamber pressure raised to the 0.8 power, which is in agreement with previous results and empirical correlations. When the maximum heat flux is fitted to the approximate form given in Eq. (7), the resulting coefficients are given in Table 2

$$q(P_c, \mathrm{O/F}) = AP_c^B + \mathrm{CO/F}^D + E \tag{7}$$

VII. Conclusions

This experiment was conducted to collect validation data for CFD models of the time-accurate, multiphase, reacting turbulent flowfield inside a multi-element oxygen/hydrogen combustor at both sub and supercritical LOX injection pressures. Recent progress in model development, validation efforts, and subscale experiments suggest that a combination of surface and integral quantities can serve as a very promising method of CFD validation, and that confidence on the validation increases with the operating range over which benchmark data are collected. To those ends, the present study collected temperature and pressure data in a highly instrumented rocket combustion chamber at 12 distinct test conditions. The temperature data collected provides not only the temperature distribution over the entire inner surface of the chamber, but the inclusion of thermocouples embedded in the chamber walls enables the computation of wall heat flux.

The axial heat flux varied from eight to 20 Btu/in.^{2}/s, with the highest heat flux occurring inline with injector elements 1–2 in. downstream from the injector face. A second peak in the offline injector measurements between two and 4 in. downstream of the injector plane suggests combination of injector plumes and outward radial flow of combustion gases. The uncertainty in heat flux is estimated to be less than 5%. The injector face heat fluxes are comparable to the wall heat fluxes in magnitude and time history, and

are well predicted by Bartz estimates. The comparison of axial heat flux profiles from multi- and single-element combustors suggests that there are significant differences in the internal flowfields. Additionally, this experiment is among the first to employ an instrumented injector face. The data from these sensors provide direct evidence of large recirculation zones in the heat end of the chamber and demonstrate the utility of common assumptions, such as Bartz approximation, concerning the magnitude of injector face heat flux.

The circumferential variation of heat flux seems to indicate the mixing and subsequent radial outflow of combustion products toward the chamber wall. This outflow brings hot combustion products into direct impinging contact with the combustor wall. Although this variation was less than 10% of the overall heat flux level, the effect was repeatable, sustained, and greater than the experimental uncertainty. Comparison of these effects with similar multi-element hardware suggests that differences in injector head configuration have a large effect on the axial heat flux profile. This indicates that, when designing a multi-element analog of a single-element chamber, maintaining geometric features like injector spacing does not yield comparable engine characteristics.

Finally, several recommendations can be made with respect to CFD validation experiments. First, the material used to construct the chamber, thermocouples, and thermocouple plugs should be from the same specimen. Second, the thermophysical characteristics of this specimen should be well characterized before the experiment over a representative range of temperatures to ensure the most accurate calculation of heat flux. With these recommendations alone, the uncertainty in heat flux could be lowered by more than a factor of 4. The design of the thermocouple plugs should allow rapid removal and replacement of failed thermocouples. The axial and circumferential locations of thermocouples should be carefully determined by considering both spatial variations in heat flux measurements and the mathematical requirements of computing heat flux profiles. Finally, the use of heat-sink cooled hardware mandates careful determination of data collection times during the test due to changes in chamber thermal condition over time.

Acknowledgments

The authors wish to extend thanks for the generous support of the NASA Constellation Universities Institute Program under Technical Contract Monitors Claudia Meyer and Jeff Rybak as well as for technical advice from Jim Hulka, Gregg Jones, Kevin Tucker, and Ron Litchford from Marshall Space Flight Center, and from Charles Merkle, Scott Meyer, Lloyd Droppers, Reuben Schuff, Nicholas Nugent, and David Helderman from Purdue, and Richard Arnold from DLR, German Aerospace Center.

References

[1] Bazarov, V. G., and Yang, V., "Liquid-Propellant Rocket Engine Injector Dynamics," *Journal of Propulsion and Power*, Vol. 14, No. 5, Sept.–Oct. 1998, p. 797. doi:10.2514/2.5343

[2] Valentine, R., Dean, L., and Pieper, J., "An Improved Method for Rocket Performance Prediction," *Journal of Spacecraft and Rockets*, Vol. 3, No. 9, Sept. 1966, p. 1409. doi:10.2514/3.28667

[3] Valentine, R. S., "Liquid Rocket Performance, Stability, and Compatibility," *Journal of Spacecraft and Rockets*, Vol. 9, No. 5, May 1972, p. 295. doi:10.2514/3.61676

[4] Wang, T., and Luong, V., "Numerical Analysis of the Hot-Gas-Side and Coolant-Stde Heat Transfer for Liquid Rocket Engine Combustors," *28th AIAA/ASME/SAE/ASEE Joint Propulsion Conference and Exhibit*, AIAA Paper 1992-3151-590, 1992.

[5] Lin, J., West, J. S., Williams, R. W., Tucker, P. K., and Chenoweth, J. D., "CFD Code Validation of Wall Heat Fluxes for a GO2/GH2 Single Element Combustor," *41st AIAA/ASME/SAE/ASEE Joint Propulsion Conference and Exhibit*, AIAA Paper 2005-4524-172, 2005.

[6] Tucker, P. K., Menon, S., Merkle, C. L., Oefelein, J. C., and Yang, V., "An Approach to Improved Credibility of CFD Simulations for Rocket Injector Design," *43rd AIAA/ASME/SAE/ASEE Joint Propulsion Conference and Exhibit*, AIAA Paper 2007-5572-459, 2007.

[7] Tucker, P. K., Menon, S., Merkle, C. L., Oefelein, J. C., and Yang, V., "Validation of High-Fidelity CFD Simulations for Rocket Injector Design," *44th AIAA/ASME/SAE/ASEE Joint Propulsion Conference and Exhibit*, AIAA Paper 2008-5226-367, 2008.

[8] Mayer, W., and Tamura, H., "Propellant Injection in a Liquid Oxygen/Gaseous Hydrogen Rocket Engine," *Journal of Propulsion and Power*, Vol. 12, No. 6, Nov.–Dec. 1996, p. 1137. doi:10.2514/3.24154

[9] Mayer, W., Schik, A., Schweitzer, C., and Schaeffler, M., "Injection and Mixing Processes in High Pressure LOX/GH2 Rocket Combustors," *32nd AIAA/ASME/SAE/ASEE, Joint Propulsion Conference and Exhibit*, AIAA 96-2620-183, 1996.

[10] Smith, J. J., Schneider, G., Suslov, D., Oschwald, M., and Haidn, O., "Steady-State High Pressure LOx/H2 Rocket Engine Combustion," *Aerospace Science and Technology*, Vol. 11, No. 1, 2007, p. 39. doi:10.1016/j.ast.2006.08.007

[11] Schumaker, S. A., and Driscoll, J. F., "Rocket Combustion Properties for Coaxial Injectors Operated at Elevated Pressures," *42nd AIAA/ASME/SAE/ASEE Joint Propulsion Conference and Exhibit*, AIAA Paper 2006-4704-644, 2006.

[12] Yeralan, S., Pal, S., and Santoro, R. J., "Experimental Study of Major Species and Temperature Profiles of Liquid Oxygen/Gaseous Hydrogen Rocket Combustion," *Journal of Propulsion and Power*, Vol. 17, No. 4, July–Aug. 2001, p. 788. doi:10.2514/2.5834

[13] Cheng, G. C., and Farmer, R., "Real Fluid Modeling of Multiphase Flows in Liquid Rocket Engine Combustors," *Journal of Propulsion and Power*, Vol. 22, No. 6, Nov.–Dec. 2006, p. 1373. doi:10.2514/1.17272

[14] Haidn, O. J., Palkina, I., Gernoth, A., and Riccius, J. R., "CFD Analysis of a Model Combustor Ignition and Comparison with Experimental Results," *43rd AIAA/ASME/SAE/ASEE Joint Propulsion Conference and Exhibit*, AIAA Paper 2007-5441-254, 2007.

[15] Masquelet, M. M., "Simulations of a Sub-Scale Liquid Rocket Engine: Transient Heat Transfer in a Real Gas Environment," M.S. Thesis, Georgia Inst. of Technology, 2006.

[16] Aeschliman, D. P., and Oberkampf, W. L., "Experimental Methodology for Computational Fluid Dynamics Code Validation," *AIAA Journal*, Vol. 36, No. 5, May 1998, p. 733. doi:10.2514/2.461

[17] Coleman, H. W., and Pal, S., "Verification and Validation in NASA-CUIP LOX/Methane Injector Research Efforts," *42nd AIAA/ASME/SAE/ASEE Joint Propulsion Conference and Exhibit*, AIAA Paper 2006-4703, 2006.

[18] Conley, A., Vaidyanathan, A., and Segal, C., "Heat Flux Measurements for a GO2/GH2 Single-Element, Shear Injector," *Journal of Spacecraft and Rockets*, Vol. 44, No. 3, May–June 2007, p. 633. doi:10.2514/1.26678

[19] Hulka, J., and Jones, G., "Comparison of Combustion Chamber Head-End Heat Flux from LO2/H2 Shear and Swirl Coaxial Injectors," *54th JANNAF Propulsion Meeting*, JANNAF, Denver, CO, 2007.

[20] Hulka, J., Jones, G., Protz, C., Bullard, B., Trinh, H., Santoro, R., Pal, S., Woodward, R., and Marshall, W., "Local Combustion Chamber Heat Flux Measurements with LO2/H2 Swirl Coaxial Injectors," *54th JANNAF Propulsion Meeting*, JANNAF, Denver, CO, 2007.

[21] Hulka, J. R., "Scaling of Performance in Liquid Propellant Rocket Engine Combustors," *20th Memorial Meeting of the Northern Section of the Japan Society for Aeronautical and Space Sciences*, NASA, 2007.

[22] Jones, G., Protz, C., Bullard, B., and Hulka, J., "Local Heat Flux Measurements with Single Element Coaxial Injectors," *42nd AIAA/ASME/SAE/ASEE Joint Propulsion Conference and Exhibit*, AIAA Paper 2006-5194, 2006.

[23] Locke, J. M., Pal, S., and Woodward, R. D., "Chamber Wall Heat Flux Measurements for a LOX/CH4 Uni-element Rocket," *43rd AIAA/ASME/SAE/ASEE Joint Propulsion Conference and Exhibit*, AIAA Paper 2007-5547, 2007.

[24] Marshall, W. M., Pal, S., Woodward, R. D., and Santoro, R. J., "Benchmark Wall Heat Flux Data for a GO2/GH2 Single Element Combustor," *41st AIAA/ASME/SAE/ASEE Joint Propulsion Conference and Exhibit*, AIAA 2005-3572, 2005.

[25] Tucker, P. K., Rybak, J. A., Hulka, J. R., Jones, G. W., Nesman, T., and West, J. S., "The NASA Constellation University Institutes Project: Thrust Chamber Assembly Virtual Institute," *42nd AIAA/ASME/SAE/ASEE Joint Propulsion Conference and Exhibit*, AIAA Paper 2006-4524, July 2006.

[26] Jones, G., Protz, C., Trinh, H., Tucker, K., Nesman, T., and Hulka, J., "Status of the Combustion Devices Injector Technology Program at the

NASA MSFC," *41st AIAA/ASME/SAE/ASEE Joint Propulsion Conference and Exhibit*, AIAA Paper 2005-4530, July 2005.

[27] Huzel, D. K., and Huang, D. H., *Design of Liquid Propellant Rocket Engines*, NASA Series S.P. 125, NASA Office of Technology Utilization, Washington, D. C., 1967.

[28] Schacht, R. L., Quentmeyer, R. J., and Jones, W. L., "Experimental Investigation of Hot-Gas Side Heat-Transfer Rates for a Hydrogen-Oxygen Rocket," NASA Technical Note TN D-2832, June 1965.

[29] Beck, J. V., Blackwell, B., and Clair, C. R. S., *Inverse Heat Conduction: Ill-Posed Problems*, Wiley–Interscience, New York, 1985.

[30] Quentmeyer, R. J., Schacht, R. L., and Jones, W. L., "Hot-Gas Side Heat Transfer with and Without Film Cooling on a Simulated Nuclear Rocket Thrust Chamber Using H2-O2," NASA Technical Note, TN D-6638, Feb. 1972.

[31] Marvin, J. G., and Holst, T. L., "CFD Validation for Aerodynamic Flows: Challenge for the 90s," *8th AIAA Applied Aerodynamics Conference*, AIAA Paper 1990-2995-386, Aug. 1990.

[32] Arnold, R., Suslov, D. I., Oschwald, M., Haidn, O. J., Aichner, T., Ivancic, B., and Frey, M., "Experimentally and Numerically Investigated Film Cooling in a Subscale Rocket Combustion Chamber," *3rd European Conference for Aerospace Sciences*, Vol. 1, No. 1, July 2009.

[33] Marvin, J. G., "Dryden Lectures in Research, A Perspective on CFD Validation," *31st Aerospace Sciences Meeting*, AIAA Paper 1993-2-516, Jan. 1993.

[34] Oberkampf, W. L., and Blottner, F. G., "Issues in Computational Fluid Dynamics Code Verification and Validation," *AIAA Journal*, Vol. 36, No. 5, May 1998, p. 687. doi:10.2514/2.456

[35] Coleman, H., and Stern, F., "Uncertainties and CFD Code Validation," *Journal of Fluids Engineering*, Vol. 119, No. 4, Dec. 1997, p. 795. doi:10.1115/1.2819500

[36] Lemmon, E. W., Huber, M. L., and Leachman, J. W., "Revised Standardized Equation for Hydrogen Gas Densities for Fuel Consumption Applications," *Journal of Research of the National Institute of Standards and Technology*, Vol. 113, No. 6, Nov.–Dec. 2008.

[37] Anon., "Measurement of Gas Flow by Means of Critical Flow Venturi Nozzles," American Society of Mechanical Engineers, MFC-7M-1987, 1987.

[38] Droppers, L., "Study of Heat Transfer in a Gaseous Hydrogen Liquid Oxygen Multi-Element Combustor," M.S. Thesis, Purdue Univ., 2007.

[39] Shampine, L., and Reichelt, M., "The MATLAB ODE Suite," *SIAM Journal on Scientific and Statistical Computing*, Vol. 18, No. 1, 1997, p. 1. doi:10.1137/S1064827594276424

[40] Skeel, R. D., and Berzins, M., "A Method for the Spatial Discretization of Parabolic Equations in One Space Variable," *SIAM Journal on Scientific and Statistical Computing*, Vol. 11, No. 1, 1990, p. 1. doi:10.1137/0911001

[41] Hensel, E., *Inverse Theory and Applications for Engineers*, Prentice Hall, Englewood Cliffs, NJ, 1991.

[42] Ozisik, M. N., and Orlande, H. R. B., *Inverse Heat Transfer*, Taylor and Francis, New York, 2000.

[43] Tikhonov, A. N., and Arsenin, V., *Solutions of Ill-Posed Problems*, edited by J. Fritz, V. H. Winston and Sons, Washington, D. C., 1977.

[44] Esposito, J., and Zabora, R., "Thurst Chamber Life Prediction: Vol I: Mechanical and Physical Properties of High Performance Rocket Nozzle Materials," NASA Technical Rept. NASA-CR-134806, 1975.

[45] White, G., and Minges, M., "Thermophysical Properties of Some Key Solids: An Update," *International Journal of Thermophysics*, Vol. 18, No. 5, 1997, p. 1269. doi:10.1007/BF02575261

E. Kim
Associate Editor